metals

MDPI

Article

Identification of Relationships between Heat Treatment and Fatigue Crack Growth of αβ Titanium Alloys

Vincent Renon [1,2], Gilbert Henaff [2,*], Céline Larignon [1,*], Simon Perusin [1] and Patrick Villechaise [2]

[1] IRT Saint Exupery, B612, 3 rue Tarfaya, CS 34436, 31405 Toulouse CEDEX 4, France; vincent.renon@ensma.fr (V.R.); simon.perusin@irt-saintexupery.com (S.P.)

[2] Institut Pprime UPR3346 CNRS ENSMA Université de Poitiers, ISAE-ENSMA, 1 Avenue Clément Ader, 86961 Futuroscope Chasseneuil CEDEX, France; patrick.villechaise@ensma.fr

* Correspondence: gilbert.henaff@isae-ensma.fr (G.H.); celine.larignon@irt-saintexupery.com (C.L.); Tel.: +33-549498233 (G.H.); +33-561006767 (C.L.)

Received: 8 March 2019; Accepted: 18 April 2019; Published: 30 April 2019

Abstract: This study deals with the influence of microstructure on the fatigue crack growth resistance of αβ titanium alloys: Ti-6Al-4V ELI (Extra Low Interstitial) that may compete with the conventional Ti-6Al-4V alloy in the manufacture of high performance aircraft. Six different microstructures have been considered: the as-received bimodal microstructures and five distinct fully lamellar microstructures. The characteristic parameters of these microstructures were determined and crack growth tests were performed with crack closure measurements in order to evaluate the shielding effect induced by closure. A comparison of crack growth rates, fracture surfaces, and crack path was carried out for the different microstructures. The results outline a transition between two propagation regimes from a microstructure-sensitive to microstructure-insensitive propagation.

Keywords: crack growth; titanium alloy; microstructure; heat treatment; crack closure

1. Introduction

Titanium alloys are nowadays widely used in structural parts in the aeronautic industry especially due to their high strength to weight ratio. Indeed, new ecological standards involve a dramatic decrease in fuel consumption and greenhouse gas emissions. Therefore weight saving in airframe applications is a key issue.

In the case of parts designed according to a damage tolerance philosophy, the improvement of the fatigue crack propagation resistance is an efficient way to get lighter parts. Meanwhile, getting deeper insights into the mechanisms involved during crack propagation in relation with the microstructure can help achieve these requirements while contributing to optimization of the material processing. It is well established that the change from a bimodal microstructure, composed of nodules and lamellae colonies, to a fully lamellar microstructure leads to a significant improvement in crack propagation resistance [1–5]. This improvement is explained by the more tortuous path of the crack through the microstructure and a higher roughness of the crack surface, leading to slower macroscopic crack propagation rates [6–8]. The influence of microstructural parameters (prior β grain and colony) of this lamellar structure has also been studied [7–9] and shows an improvement of damage resistance with increasing prior β grain or colony size.

In this study, the potential use of the Ti-6Al-4V ELI alloy is considered. This alloy may compete with the conventional Ti-6Al-4V alloy to manufacture high performance, damage-tolerant aircraft components, provided that superior fatigue crack growth properties could be achieved by proper heat treatments without substantial degradation of other properties.

To change the microstructure from bimodal to fully lamellar, different heat treatments above the beta transus were tested on Ti-6Al-4V ELI. The generated microstructures were characterized in terms of ex-β grain size, lamellar colony thickness, and lamellae thickness as well as crack propagation resistance properties. The fatigue crack growth test data were then analyzed with special attention paid to shielding effects induced by crack closure which might contribute to improving crack propagation properties. Observations of the different propagation mechanism in action, in combination with analysis of different shielding effects, were used to improve the understanding of the impact of microstructure modifications on crack propagation in Ti-6Al-4V. Differences in propagation regimes in lamellar microstructures, before and after the outlined transition, were also studied.

2. Materials and Methods

The samples were machined by electrical discharge machining from a billet (R = 90 mm, L = 1 m) provided by TIMET (Ugine, France) and forged in the alpha–beta domain. The measured chemical composition (in weight %) of this billet is given in Table 1. The β transus temperature was evaluated, according to chemical composition, at 980 °C.

Table 1. Measured chemical composition of the Ti-6Al-4V ELI alloy under study.

Aluminum	Vanadium	Carbon	Iron	Oxygen	Nitrogen	Hydrogen	Titanium
6.24	3.97	0.015	0.16	0.12	0.002	<0.003	Balance

Slices of 50 mm were cut in the billet and submitted to different heat treatments. The slices of billet were sized so as to collect, in each piece, 3 CT40 B10 specimens. The sampling draft was determined in order to avoid near surface areas which could have been chemically affected by heat treatment, especially oxygen enrichment from the external surface.

Heat treatments were performed in a Nabertherm 1750 furnace (Nabertherm, Lilienthal, Germany). The temperature was monitored by an S-type thermocouple (TCDirect, Dardilly, France). The thermocouple was calibrated prior to the treatment and then placed in a 10 mm deep and 1.5 mm in diameter hole drilled in the treated slice of material, in order to get a measurement representative of the temperature inside the slice, near the point where CT specimens will be machined (Figure 1).

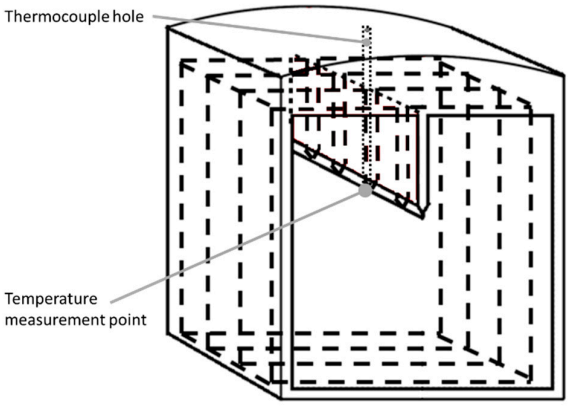

Figure 1. Slice of billet for heat treatment with a thermocouple hole and the position of CT sample collection.

CT samples and pieces for microstructural analysis were collected from treated slices. Specimens were polished on both main faces with up to SIC4000 paper. Their dimensions were precisely measured. Crack closure was measured with the back face gauge presented in Figure 2

Fatigue crack propagation tests were conducted with an Instron 8501 hydraulic testing machine, with a ±25 kN load cell, in laboratory air at room temperature at a load ratio of $R = 0.1$ and a frequency of 20 Hz. The test frequency was periodically (every 5000 cycles) reduced to 0.2 Hz for 20 cycles in order to perform crack closure measurements. The crack length was monitored by means of a potential drop method. The principle of this method is shown in Figure 2. A constant direct current is introduced in the sample. After a calibration, the voltage evolution at the crack edges is related to the crack propagation.

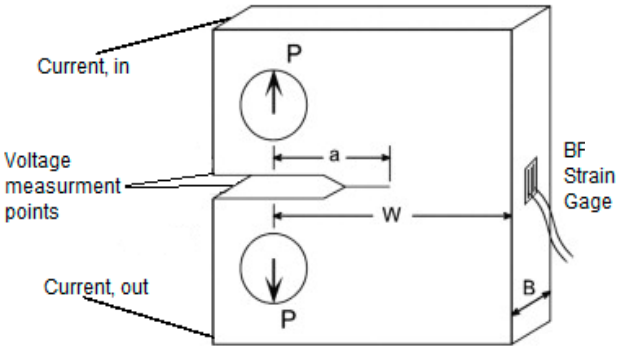

Figure 2. Potential drop method principle with a back face (BF) strain gage.

The precracking was carried out at $R = 0.1$ and a constant stress intensity range $\Delta K = 12$ MPa√m. After precracking, this level of ΔK was used as the initial value for the constant load amplitude crack propagation test.

For every test, closure measurements as defined by Kikukawa [10] were performed, through a back face strain gage (Figure 2). Thanks to these measurements the effective stress intensity range was calculated as defined by Elber [11]:

$$\Delta K_{\text{eff}} = U \times \Delta K \quad (1)$$

with $U = \frac{P\text{max} - P\text{op}}{P\text{max} - P\text{min}}$. *Pop* is defined as the load at which the curve of back face strain versus load lost linearity during the unloading portion of the cycle. This nonlinearity is characteristic of the contact between crack faces.

The effective stress intensity range will be used to plot crack growth curves in order to isolate the specific microstructural influence on crack tip damage from shielding induced by closure.

For two of the microstructures, additional tests were performed at a load ratio of $R = 0.7$.

A quantitative microstructural characterization of the microstructures generated was performed. The heat treated microstructures of the Ti-6Al-4V ELI were characterized with a Jeol 6400 SEM (Jeol, Croissy Sur Seine, France) and a Zeiss axio imager Z2 optical microscope (Zeiss, Marly le roi, France), after mirror polishing and Kroll's reagent etching. SEM images were used to determine the thickness of lamellae and of lamellar colonies, while polarized optical images were used to quantify the prior β grain size. These prior β grain size values were determined using the intercept method described in ASTM E112 [12]. Lamellae and colony mean sizes were estimated with direct measurements of the thickness on the images. These measurements were performed on multiples pictures at different locations of samples to get a representative value of the average microstructure of the sample. In practice, an average over 100 colonies, from at least 25 different locations and ex-β grains were measured for a given lamellar microstructure. Furthermore, at least 1000 lamellae from 100 different colonies were measured to get the average thickness of the lamellae.

After crack propagation testing, observations of the fracture surface and of the crack path, both at different ΔK levels, were performed. One half of the cracked sample was used for the observation

of the fracture surface. The other half of the specimen was cut to get access to the crack path at mid-thickness. The crack paths and fracture surfaces were both observed by SEM.

Additional characterizations were performed with Alicona infinite focus to get 3D topology of cracked surfaces. These 3D surfaces were used to measure crack path deviation.

3. Microstructure Generation

Six different microstructures were considered in this study. The first one was the initial bimodal microstructure from the αβ forged billet. This as-received bimodal microstructure was almost equiaxed, with an average grain size of 16 μm, and was composed of approximately 5% lamellar colonies as shown in Figure 3.

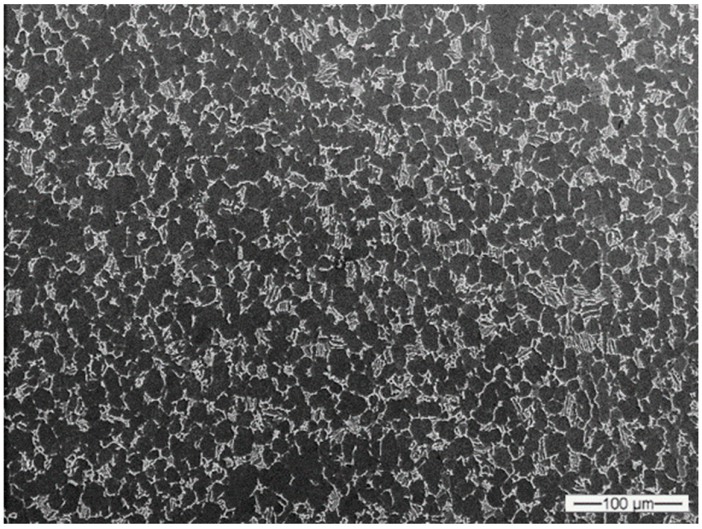

Figure 3. As-received bimodal microstructure.

From this initial bimodal microstructure, five lamellar microstructures were generated by means of different heat treatments. Particular attention was paid to the monitoring of the cooling rate so as to obtain a representative value of the actual cooling rate measured on a billet in industrial conditions. A schematic representation of these five heat treatments is shown in Figure 4. The first one was a solution annealing at T_β + 25 °C for 1h 30 min, followed by ageing at 730 °C for 1 h. Two additional treatments were derived by a modification in the solution annealing duration, which was 2 h 15 min in one case and 3 h for the other one. Finally the last two consisted of a modification in the solution annealing temperature with T_β + 50 °C and T_β + 75 °C for a duration of 1 h 30 min. A schematization of all heat treatments performed is shown in Figure 4.

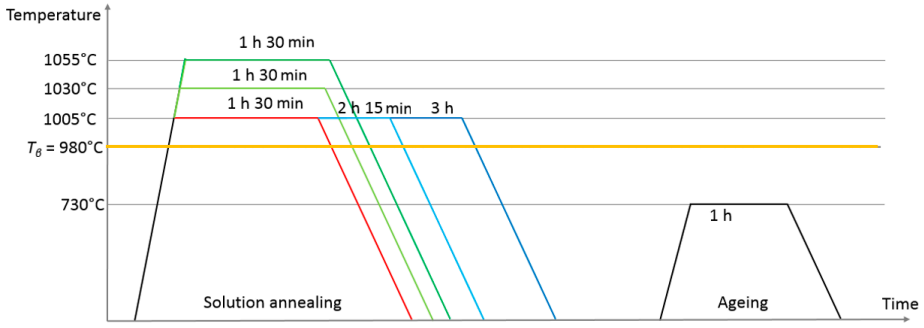

Figure 4. Heat treatments performed.

Some examples of the resulting microstructures are presented in Figures 5–7, with both polarized optical (A) and SEM (B) pictures. From these figures, it appears that the increase in either

the annealing temperature or the duration above the beta transus temperature leads to an increase in size of both the lamellae and of the ex-β grains.

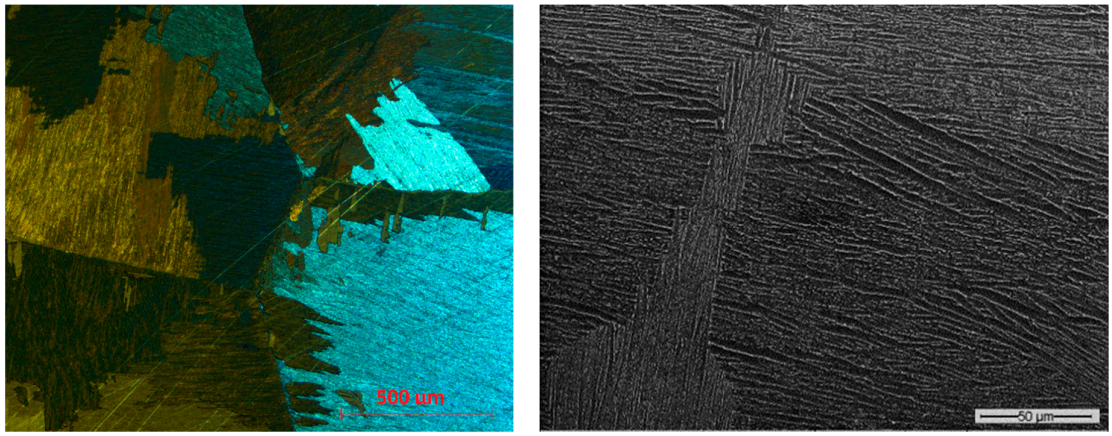

(**a**) (**b**)

Figure 5. Lamellar microstructure obtained with annealing temperature T_β + 25 °C for 1 h 30 min, viewed with polarized optical microscopy (**a**) and SEM (**b**).

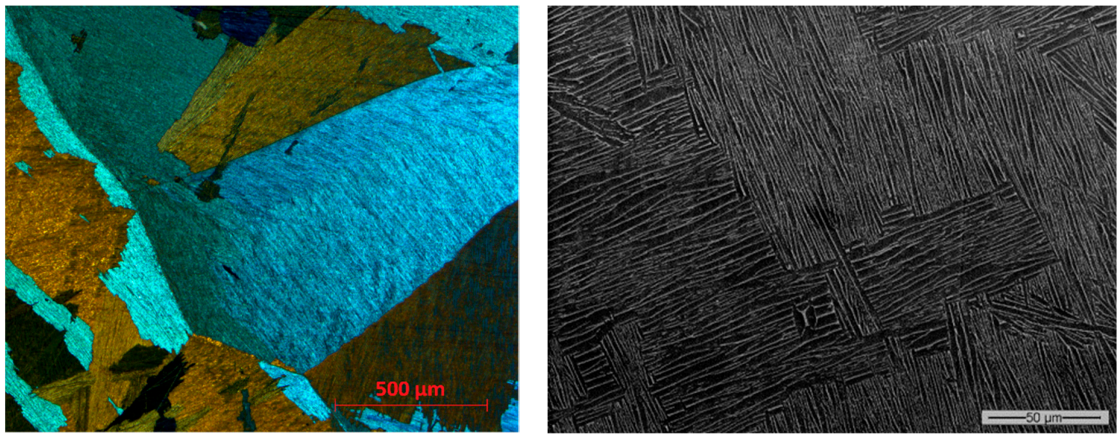

(**a**) (**b**)

Figure 6. Lamellar microstructure obtained with annealing temperature T_β + 25 °C for 3 h, viewed with polarized optical microscopy (**a**) and SEM (**b**).

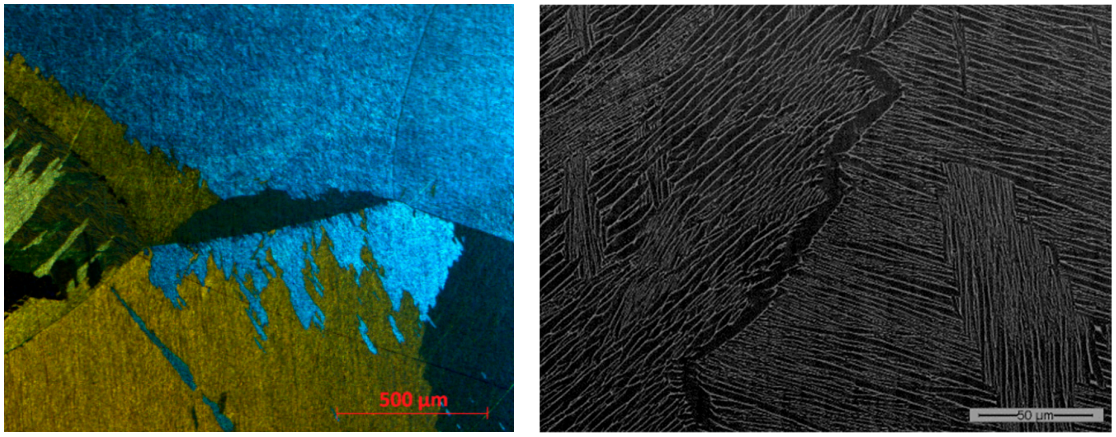

(**a**) (**b**)

Figure 7. Lamellar microstructure obtained with annealing temperature T_β + 75 °C for 1 h 30 min, viewed with polarized optical microscopy (**a**) and SEM (**b**).

A statistical analysis of the main microstructural features was performed in order to provide representative data of the microstructures generated. The results are presented in Table 2. This analysis revealed that the main difference between the five microstructures lies in the prior β grain size. Indeed, this microstructural parameter increased with the duration or temperature of the solution annealing step. Typically, a rise in the heat treatment temperature of 25 °C or duration of 45 min led to a coarsening of ex-β grain size of approximately 26%, and doubling the duration of heat treatment resulted in a coarsening of ex-β grain size of 31%. The most significant increase was measured for a rise of heat treatment temperature of 50 °C to T_β + 75 °C which resulted in an increase of ex-β grain size of 37%.

Table 2. Lamellar microstructure parameters.

Heat Treatment (Duration/Temperature)	Ex-β Grain Size (μm)		Lamellar Colony Size (μm)		Lamellae Width (μm)	
	Value	Standard Deviation	Value	Standard Deviation	Value	Standard Deviation
T_β + 25 °C 1 h 30 min	1283	108	461	292	1.25	0.28
T_β + 25 °C 2 h 15 min	1615	58	466	294	1.24	0.32
T_β + 25 °C 3 h	1686	101	425	225	1.46	0.42
T_β + 50 °C 1 h 30 min	1614	99	508	239	1.22	0.36
T_β + 75 °C 1 h 30 min	1764	215	436	283	1.35	0.43

The results in Table 2 show that the measurements of lamellar colony sizes lead to a high standard deviation. In fact, the variation in the measurements of colony dimensions is very important, with a measured size varying between approximately 100 and 1000 μm. By considering these deviations, it can be concluded that the size of the lamellar colonies and the width of the lamellae cannot be monitored by a modification of either the temperature or the duration of the β-heat treatment. The prior β grain size is therefore the only parameter that is significantly modified by a higher solution annealing temperature or duration, with coarser ex-β grains found after heat treatment with longer or higher solution annealing.

Static properties of initial and heat-treated materials were obtained by two tensile tests on each microstructure. The results of these tests are presented on Figure 8 and Table 3. The first observation is the important difference between bimodal and lamellar microstructures. Indeed the maximum stress and the elongation at failure were significantly higher for the bimodal microstructure. This observation is confirmed by the data in the Table 3. The yield stress was also higher for the bimodal microstructure. On the other hand, a modification from bimodal to lamellar microstructure did not affect the Young's modulus.

The second observation is that all the lamellar microstructures exhibited a similar behavior which was furthermore different from the one observed in the bimodal microstructure. Indeed the bimodal structure showed a moderate strain hardening prior to necking. The curves obtained with the lamellar microstructures presented almost no hardening after the yielding point on the conventional curves, leading to observation of plastic consolidation on the rational curves.

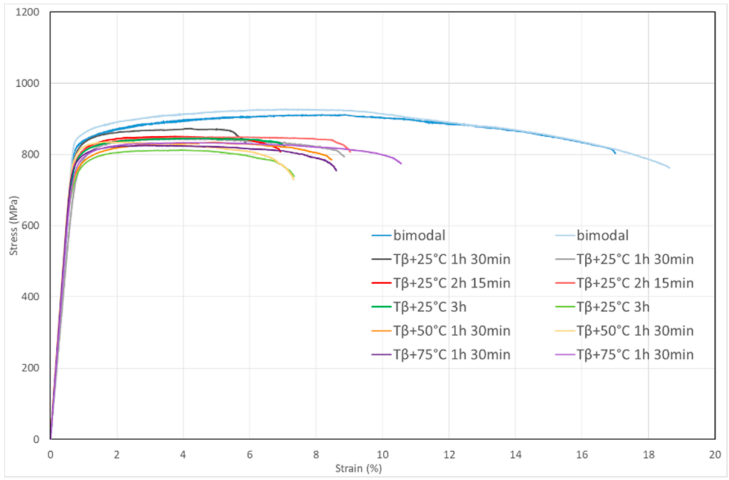

(**a**)

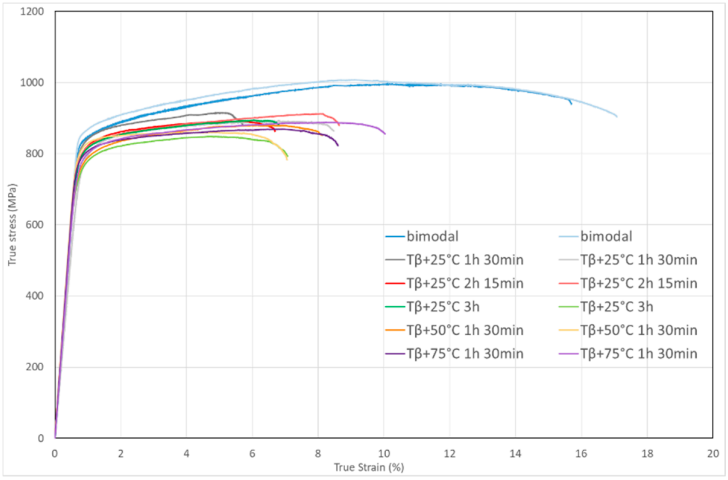

(**b**)

Figure 8. Engineering (**a**) and True (**b**) stress strain curves of the six microstructures.

Table 3. Mean static properties of the six microstructures.

Heat Treatment (Duration/Temperature)	E (GPa)		Rp 0.2 (MPa)		Rm (MPa)		A%	
	Value	Standard Deviation	Value	Standard Deviation	Value	Standard Deviation	Value	Standard Deviation
As received (bimodal)	121	3	848	11	1001	5.5	15.6	0.75
Tβ + 25 °C 1 h 30 min	114	9	803	23	904	11.5	6.5	1.35
Tβ + 25 °C 2 h 15 min	125	1.5	803	1.5	902	10.5	7.4	1.15
Tβ + 25 °C 3 h	123	0	776	24	871	23	6.4	0.1
Tβ + 50 °C 1 h 30 min	124	3.5	790	24	869	10	7.0	0.45
Tβ + 75 °C 1 h 30 min	124	1.5	786	4.5	878	10	8.8	0.65

These results, especially the yield stress, are used for the calculation of plastic zone sizes during the crack propagation test.

4. Results

The fatigue crack propagation rates are plotted in Figure 9 with respect to the stress intensity range ΔK. As expected from the literature survey [1–3], despite a larger scatter in results obtained at low ΔK values, the lamellar microstructures exhibited a higher fatigue crack propagation resistance than the bimodal structure. In addition the five lamellar microstructures studied showed a nearly similar behavior with a superior resistance up to ΔK = 50 MPa√m as compared to the bimodal microstructure. Comparison with standard Ti-6Al-4V crack propagation properties showed that ELI grade did not show significant improvement in crack propagation properties.

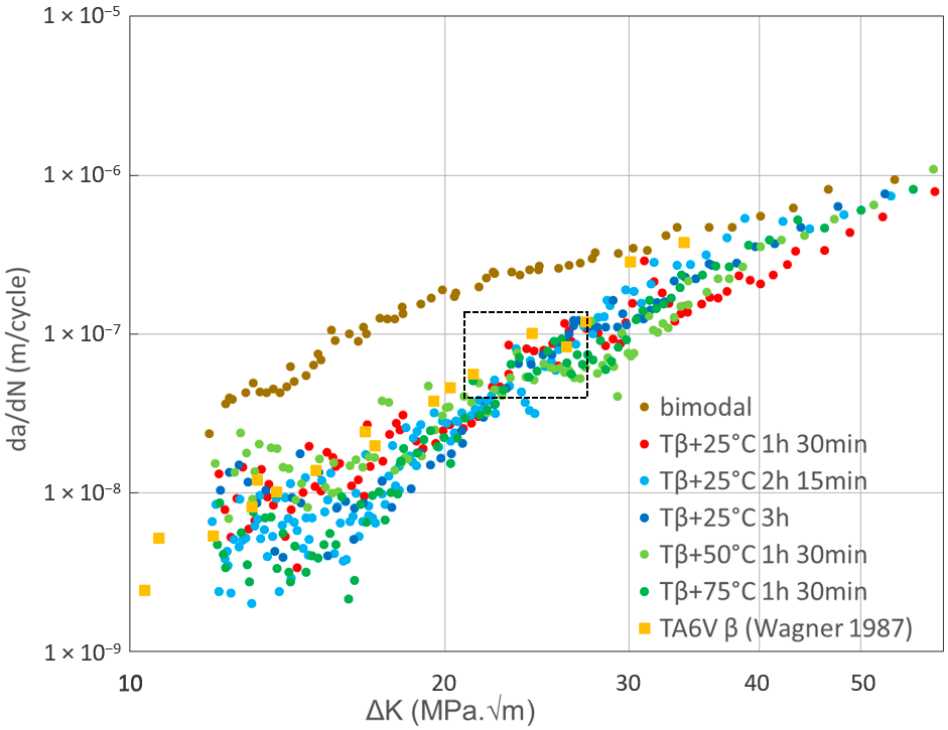

Figure 9. Crack propagation rates da/dN versus ΔK for the six different microstructures of Ti-6Al-4V ELI compared with the lamellar microstructure of standard Ti-6Al-4V, data from [13].

Furthermore, for these lamellar microstructures, two characteristic propagation regimes can be identified, each one characterized by a specific slope in the da/dN curve. The transition point between these two regimes can be estimated to approximately ΔK_T = 25MPa√m and is identified in Figure 9 by the dotted rectangle.

Such a transition was previously reported in literature [2,9,14] and was attributed to the point where the cyclic plastic zone size is equal to the average lamellar colony size.

Examples of crack paths and fracture surfaces before and after this transition (Figure 10) are shown in the Figure 11; Figure 12, at ΔK = 20 MPa√m (Figures 11a and 12a) and at ΔK = 40 MPa√m, respectively (Figures 11b and 12b).

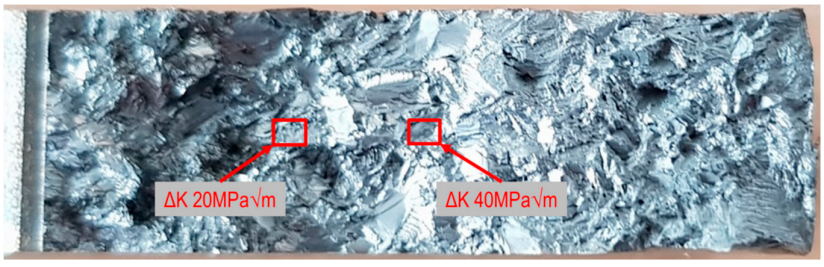

Figure 10. Positions of Figure 11; Figure 12 observation position.

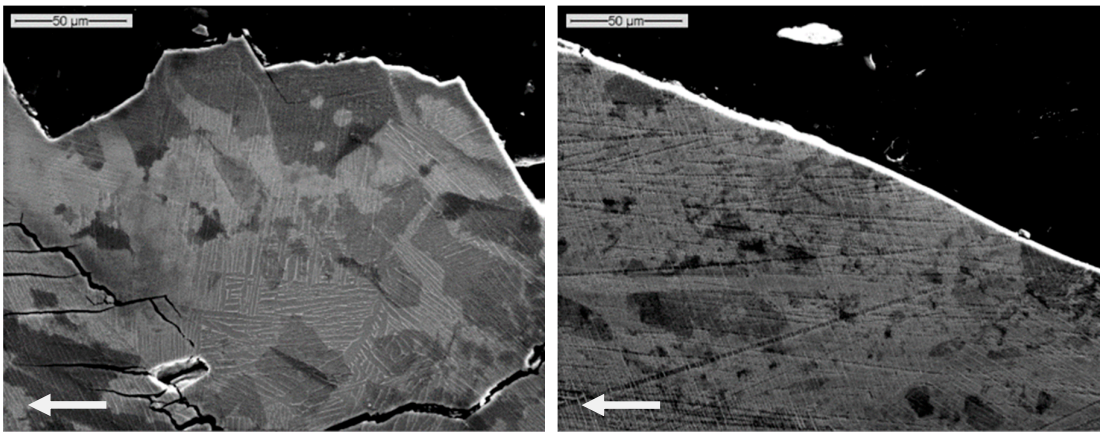

(**a**) (**b**)

Figure 11. Crack path at mid-thickness before (**a**) and after (**b**) transition, respectively at ΔK = 20 MPa√m and at ΔK = 40 MPa√m, T_β + 75 °C for 1 h 30 min heat treatment, propagation according to the arrow.

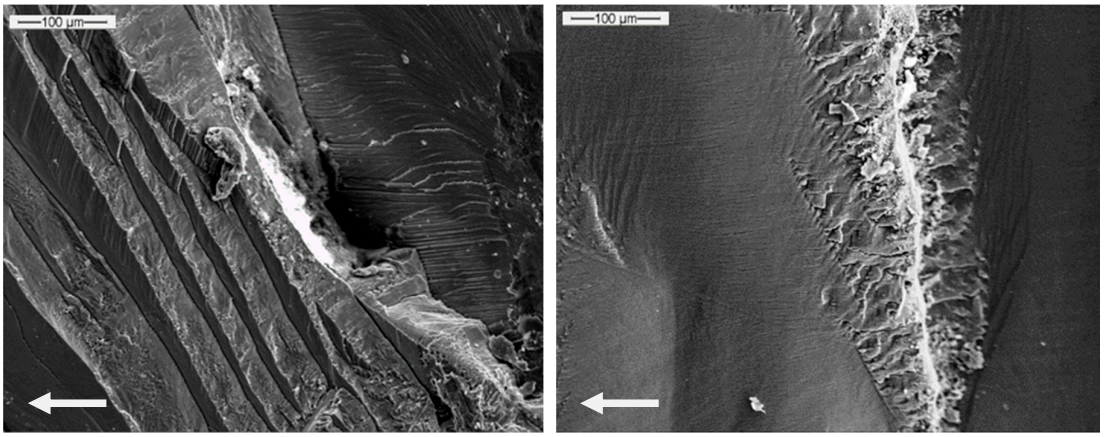

(**a**) (**b**)

Figure 12. Crack surface at mid-thickness before (**a**) and after (**b**) transition, respectively at ΔK = 20 MPa√m and at ΔK = 40 MPa√m, T_β + 75 °C for 1 h 30 min heat treatment, propagation according to the arrow.

In these pictures, a clear difference can be noticed between the two ΔK values selected on both sides of the transition, respectively ΔK = 20 MPa√m and ΔK = 40 MPa√m, in the crack path and the fracture surface. Indeed, the crack path before transition (Figure 11a) exhibited an important deflection and associated roughness, associated to crystallographic propagation, while beyond the transition point the path was far smoother and had less deflection (Figure 11b). It should also be noticed that there was an important presence of secondary cracks before the transition whereas no secondary crack was found after transition.

The comparison of the fracture surfaces in Figure 12 was consistent with these observations of crack paths. Thus the crack surface before transition (Figure 12a) showed an important relief associated with the crystallographic propagation mode [14] characterized by the presence of many facets and propagation by steps with important bifurcation of crack propagation between two facets. After transition (Figure 12b) the crack surface presented less relief and propagation did not seem to follow specific crystallographic plans.

The closure results for the bimodal and three lamellar microstructures are displayed in Figure 13 with the U ratio as defined by Elber is plotted as a function of ΔK.

Again, it can be seen that the behavior of the bimodal microstructure was different from that exhibited by the lamellar microstructures, which in turn presented a similar behavior between each other. More precisely, the variation in solution annealing temperature had no effect on the opening stress, as indicated by the superposition of the curves for T_β + 25 °C 1 h 30 min and T_β + 75 °C 1 h 30 min. The curve for T_β + 25 °C 3 h showed, however, a slight difference from the two other heat treated samples. On these lamellar microstructures three phases were distinguished. The first one, which lies between ΔK = 12 MPa√m and approximately ΔK = 15 MPa√m, was characterized by a decrease in the value of the U ratio as the ΔK increased. This decrease could be caused by the development of the roughness-induced closure at the beginning of the propagation.

From this stage up to approximately ΔK = 30 MPa√m (at higher ΔK for the T_β + 25 °C 3 h) the closure was slowly reduced before reaching a constant level. This higher U value represented a reduction in the shielding effect induced by closure. It happened shortly after the transition and could be related to the change from a crystallographic propagation mode, characterized by a rough fracture surface, to a stage II propagation regime beyond the transition suspected from fracture surface analysis. Indeed, crystallographic propagation before transition generated a high roughness of the fracture surface and by this means promoted roughness-induced closure [15].

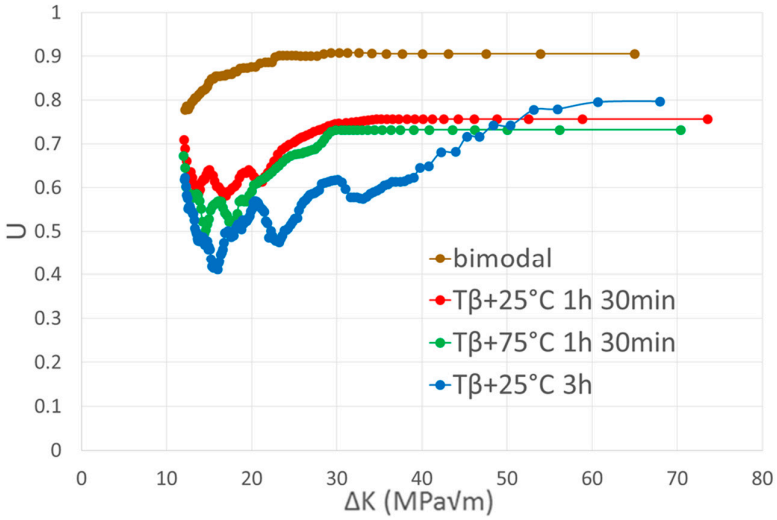

Figure 13. Crack closure measurements for three lamellar microstructures and the bimodal microstructure.

On the basis of these crack closure measurements, crack growth rates were plotted as a function of ΔK and the effective stress intensity range (ΔK_{eff}) in Figure 14 for the bimodal microstructure and one lamellar microstructure. In the following section, only one lamellar microstructure was selected for time saving purposes, more precisely the one obtained after T_β + 25 °C/3h heat treatment. This plot also includes data obtained at a load ratio R = 0.7. This high mean stress loading generated a larger monotonic plastic zone size at the crack tip without modification of the cyclic plastic zone for a given ΔK value, so as to distinguish the effects of cyclic plasticity from the effects induced by monotonic plasticity at the crack tip, in particular their role in controlling the transition. It is also noteworthy that, as expected, no crack closure effect was detected during the tests at a load ratio of R = 0.7, so that the ΔK_{eff} value can be considered as equal to ΔK.

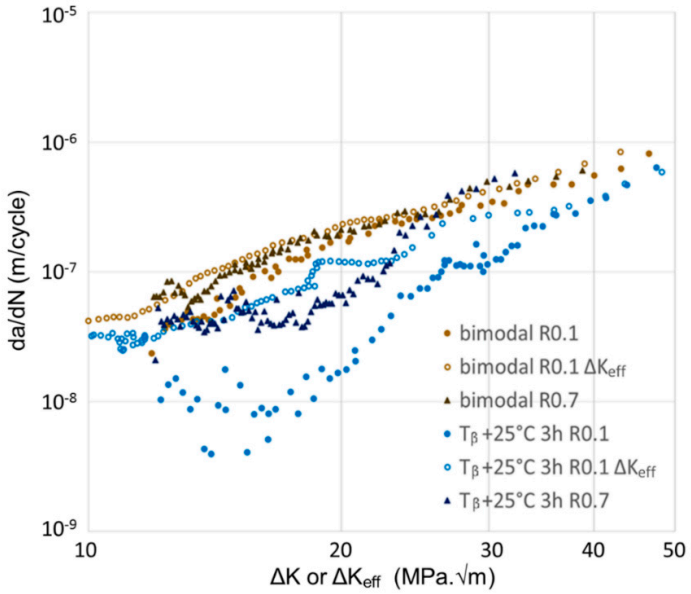

Figure 14. Fatigue crack propagation rates as a function of effective stress intensity range ΔK_{eff} at R = 0.1 and R = 0.7 tests of the bimodal microstructure and one lamellar microstructure.

Several conclusions can be drawn from Figure 14. The first point is that, even by taking into account the shielding induced by crack closure when expressing the growth rates as a function of effective stress intensity range, it appeared that the lamellar microstructure still presented a higher resistance to crack propagation than the bimodal microstructure. The difference between the bimodal and lamellar microstructure was however reduced, indicating that differences in the intensity of closure effects were partially responsible for the differences in crack growth resistance, but this does not fully account for the observed difference.

The second observation is that for a load ratio of R = 0.7, the results for bimodal microstructure were identical to the one with an effective stress intensity range at R = 0.1. The lamellar microstructure at R = 0.7 also showed similar behavior, with results quite similar to the results of crack growth rates as a function of an effective stress intensity range at R = 0.1. At R = 0.7 the transition was also visible at ΔK ~25 MPa√m, which was, unlike what was seen in the bimodal microstructures [16], the same ΔK value at R = 0.1. This transition between two propagation regimes, also observed when considering ΔK_{eff} at R = 0.1 was confirmed to be related to the cyclic deformation as proposed by Wanhill [17].

By considering the difference in crack surface roughness between the two types of microstructures, the cause of the remaining difference between the two microstructures after removing the crack closure effects could be the length of crack wake. Indeed, with a higher roughness, one can imagine that the developed surface of the crack will be higher in lamellar microstructures than in bimodal ones. This effect could lead to a lower macroscopic crack propagation rate as explained by Yoder [14].

The high roughness of lamellar microstructures could also lead to a mixed mode I and mode II propagation. The identification of the respective contribution of mode I and mode II to the crack driving force was done using the model proposed by Suresh [18]:

$$k_1 = a_{11}(\theta)K_I + a_{12}(\theta)K_{II} \quad (2)$$

$$k_2 = a_{21}(\theta)K_I + a_{22}(\theta)K_{II} \quad (3)$$

With θ the deflection angle of the propagation surface with respect to the macroscopic propagation plan. In the present case study, $K_{II} = 0$, so only $a_{11}(\theta)$ and $a_{21}(\theta)$ were considered. They are defined by Suresh as follows:

$$a_{11}(\theta) = \cos^3\left(\frac{\theta}{2}\right) \quad (4)$$

$$a_{21}(\theta) = \sin\left(\frac{\theta}{2}\right)\cos^2\left(\frac{\theta}{2}\right) \quad (5)$$

Finally the effective stress intensity factor is defined as:

$$K_{\mathrm{eff,S}} \approx \sqrt{{k_1}^2 + {k_2}^2} \quad (6)$$

From these equations, the effective stress intensity factor as defined by Suresh, $K_{\mathrm{eff,S}}$, can be calculated. 3D measurement of the crack surface was performed on lamellar microstructures, as illustrated on Figure 15.

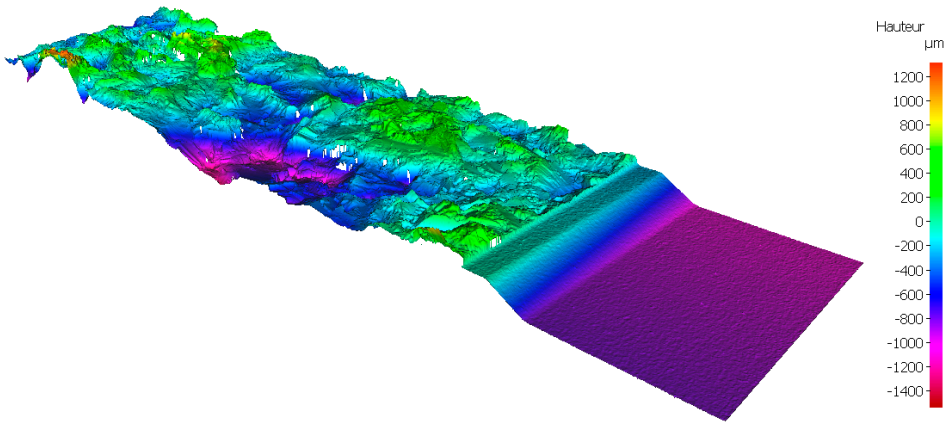

Figure 15. 3D measurement of the crack surface.

The average deflection angle of the crack path, representing the angle between the cracked surface and the average propagation plan, before and after transition were measured in this 3D mapping. Resulting values were an average deflection of 42° before transition and 29° after transition. These averaged angles were then used to compute $K_{\mathrm{eff,S}}$ and therefore $\Delta K_{\mathrm{eff,S}}$.

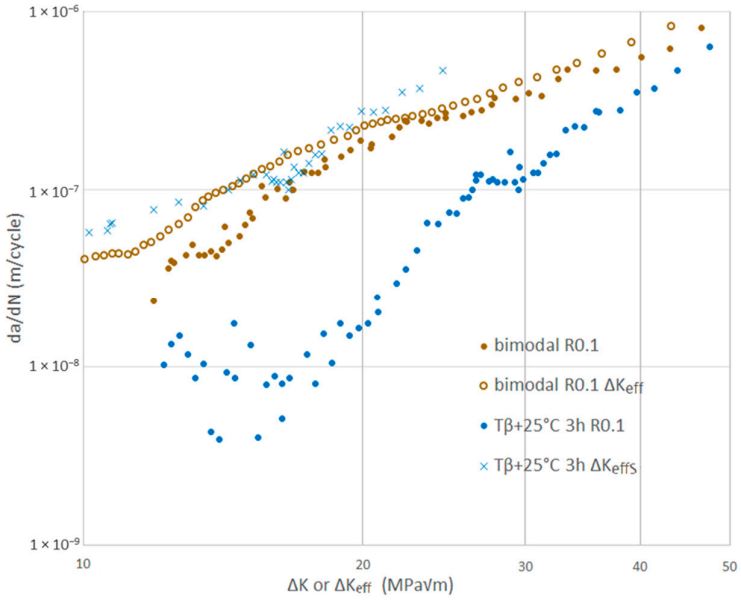

Figure 16. Fatigue crack propagation rates as a function of effective stress intensity range ΔK_{eff} and ΔK_{effS} at $R = 0.1$ for one lamellar microstructure, compared to the bimodal microstructure.

The results of this analysis are presented in Figure 16. It was visible that using both the crack closure correction and the Suresh model for deviation, the difference between bimodal and lamellar microstructure was suppressed, with a good correlation between lamellar da/dN vs. $\Delta K_{eff,S}$ and bimodal da/dN vs. ΔK_{eff} curves. This correlation showed that the difference between bimodal and lamellar microstructures can be fully explained by crack deviation and closure. This correlation could be enhanced by performing additional measurements of the average deviation angle at smaller ΔK values (in this study two measurements were performed, one for a range of ΔK from 12 to 25 MPa√m, the second for ΔK from 25 to 50 MPa√m).

5. Conclusions

In this study, the impact of heat treatment on microstructural characteristic parameters of typical lamellar microstructures of a Ti-6Al-4V ELI alloy and the consequences on fatigue crack propagation resistance were investigated. The following conclusions can be drawn from the analysis of the results:

1 The duration and the temperature above the beta transus of the solution-annealing step have an impact on the resultant microstructure. The main impact identified is the ex-β grain coarsening, with a limited impact on lamellar colony size, whereas no impact was evidenced on lamellae size. The increase in temperature from T_β + 25 to T_β + 75 or duration from 1 h 30 min to 3 h resulted in an increase in ex-β grain growth of about 30–40%.

2 As previously seen for standard Ti-6Al-4V, the Ti-6Al-4V ELI lamellar microstructures generated by β heat treatments presented superior fatigue crack propagation properties as compared to the bimodal microstructure, especially for $\Delta K < \Delta K_T$. However the difference in prior β grain size had no influence on the resistance of lamellar microstructures.

3 The differences in fatigue crack propagation properties between lamellar and bimodal microstructures can be partially accounted for by crack closure effects. The roughness of crack surfaces can explain the remaining difference by generating mixed mode I and mode II propagation. Using both crack closure correction and the Suresh model for mixed mode propagation, the difference between the two microstructure can be fully explained.

4 Two characteristic fatigue crack propagation regimes with a transition point were observed on lamellar microstructures for R = 0.1 and for R = 0.7. The cracks tended to grow along crystallographic planes before the transition, generating the high fracture surface roughness and a lot of secondary cracks, while microstructure had less effect after transition with crack without important deflections. The ΔK_T value at the transition was the same at R = 0.1 and R = 0.7, confirming that the transition was mainly controlled by cyclic plasticity.

This last point is currently under more detailed investigation in order to get deeper insights about the near-tip plasticity of this transition regime using in situ SEM tensile tests coupled with EBSD acquisition at specific ΔK values (20 and 40 MPa√m). These in situ tests will be performed on micro samples machined in the crack tip region of the CT sample tested under constant ΔK interrupted tests. The objective is to observe the deformation process in relation to local deformation mechanisms at the crack tip during loading. Meanwhile, EBSD analysis of crack paths will be carried out in order to precisely identify the crystallographic nature of crack growth.

Author Contributions: Conceptualization, V.R., G.H., C.L., S.P., and P.V.; methodology, V.R.; validation, V.R., G.H., C.L., S.P., and P.V.; formal analysis, V.R.; investigation, V.R.; resources, G.H., C.L., S.P., and P.V.; data curation, V.R..; writing—original draft preparation, V.R.; writing—review and editing, G.H., C.L., S.P., and P.V.; visualization, V.R.; supervision, G.H., C.L., S.P., and P.V.; project administration, G.H., C.L., S.P., and P.V.

Acknowledgments: This work has been performed in the frame of the IRT Saint-Exupéry-Metaltechnics project. The authors would like to thank all members of the Metaltechnics project and in particular Airbus Operations, Aubert and Duval, and Timet for their support.

Conflicts of Interest: The authors declare no conflict of interest.

References

1. Nalla, R.K.; Ritchie, R.O.; Boyce, B.L.; Campbell, J.P.; Peters, J.O. Influence of microstructure on high-cycle fatigue of Ti-6Al-4V: Bimodal vs. lamellar structures. *Metall. Mater. Trans. A* **2002**, *33*, 899–918.
2. Irving, P.E.; Beevers, C.J. Microstructural influences on fatigue crack growth in Ti-6Al-4V, *Mater. Sci. Eng.* **1974**, 14, 229–238.
3. Hadj Sassi, B.; Lehr, P. Ténacité et résistance à la propagation des fissures de fatigue de l'alliage de titane TA6V, *J. Less-Common Met.* **1997**, *56*, 157–165.
4. Laziou, J. Influence de la structure sur les propriétés mécaniques, la ténacité et la tenue à la fatigue de l'alliage de titane TA6V, *J. Less-Common Met.* **1976**, *46*, 129–249.
5. Krüger, L.; Grundmann, N.; Trubitz, P. Influence of Microstructure and Stress Ratio on Fatigue Crack Growth in a Ti-6-22-22-S alloy, *Mater. Today: Proc.*, **2015**, *2*, S205–S211.
6. Walker, K.; Wang, C.H.; Newman Junior, J. C. Fatigue Crack Closure due to Surface Roughness and Plastic Deformation, *Adv. Mater. Res.* **2014**, *891–892*, 319–324.
7. Eylon, D. Faceted fracture in beta annealed titanium alloys, *Metall. Trans. A.* **1979**, *10*, 311–317.
8. Qiu, J.; Feng, X.; Ma, Y.; Lei, J.; Liu, Y.; Huang, A.; Rugg, D.; Yang, R. Fatigue crack growth behavior of beta-annealed Ti–6Al–2Sn–4Zr–xMo (x = 2, 4 and 6) alloys: Influence of microstructure and stress ratio, *Int. J. Fatigue* **2016**, *83*, 150–160.
9. Yoder, G.R.; Cooley, L.A.; Crooker, T.W. Quantitative analysis of microstructural effects on fatigue crack growth in widmanstätten Ti-6A1-4V and Ti-8Al-1Mo-1V, *Eng. Fract. Mech.* **1979**, *11*, 805–816.
10. Kikukawa, M.; Jono, M.; Mikami, S. Fatigue Crack Propagation and Crack Closure Behavior under Stationary and Varying Loadings (Test Results of Aluminum Alloy). *J. Soc. Mater. Sci. Jpn.* **1982**, *31*, 483–487.
11. Elber, W. Fatigue crack closure under cyclic tension. *Eng. Fract. Mech*. **1970**, *2*, 37–45.
12. ASTM international. *ASTM E112-12 Standard Test Methods for Determining Average Grain Size*; ASTM International: West Conshohocken, PA, USA, 2013.
13. Wagner, L.; Lutjering, G. Microstructural Influence on Propagation Behavior of Short Cracks in an (alpha + beta) Titanium Alloy. *Z. Metallkd.* **1987**, *78*, 369–375.
14. Yoder, G.R.; Cooley, L.A.; Crooker, T.W. Fatigue Crack Propagation Resistance of Beta-Annealed Ti-6Al-4V Alloys of differing interstitial oxygen contents. *Metall. Trans. A* **1978**, *9A*, 1413–1420.
15. Wanhill, R.; Barter, S. *Fatigue of Beta Processed and Beta Heat-treated Titanium Alloys*; Springer: Dordrecht, The Netherlands, 2012.
16. Wanhill, R. Material-based failure analysis of a helicopter rotor hub; ASM International: Geauga County, OH, USA, 2003.
17. Wanhill, R.J.H.; Galatolo, R.; Looije, C.E.W. Fractographic and microstructural analysis of fatigue crack growth in a Ti-6A1-4V fan disc forging. *Int. J. Fatigue* **1989**, *17*, 407–416.
18. Suresh, S. Crack deflection: Implications for the growth of long and short fatigue cracks. *Metall. Trans. A* **1983**, *14*, 2375–2385.